

Emergent, Non-Aging, Extendable, and Rechargeable Exchange Bias in 2D Fe₃GeTe₂ Homostructures Induced by Moderate Pressuring

Caixing Liu, Huisheng Zhang, Shunhong Zhang, De Hou, Yonglai Liu, Hanqing Wu, Zhongzhu Jiang, HuaiXiang Wang, Zongwei Ma, Xuan Luo, Xiaoyin Li, Yuping Sun, Xiaohong Xu, Zhenyu Zhang,* and Zhigao Sheng*

As a crucial concept in magnetism and spintronics, exchange bias (ExB) measures the asymmetry in the hysteresis loop of a pinned ferromagnet (FM)/antiferromagnet (AFM) interface. Previous studies are mainly focused on FM/AFM heterostructures composed of conventional bulk materials, whose complex interfaces prohibit precise control and full understanding of the phenomenon. Here, the enabling power of 2D magnets is exploited to demonstrate the emergence, non-aging, extendability, and rechargeability of ExB in van der Waals Fe₃GeTe₂ homostructures, upon moderate pressuring. The emergence of the ExB is attributed to a local stress-induced FM-to-AFM transition, as validated using first-principles calculations, and confirmed in magneto-optical Kerr effect and second harmonic generation measurements. It is also observed that, negligible ExB aging before the training effect suddenly takes place through avalanching, pronounced delay of the avalanche via timed pressure repetition (extendability), ExB recovery in the post-training sample upon refreshed pressuring (rechargeability), and demonstrate its versatile tunability. These striking findings offer unprecedented insights into the underlying principles of ExB and its training, with immense technological applications in sight.

1. Introduction

When an exchange anisotropy is present at the interface of an antiferromagnet (AFM) and ferromagnet (FM) layer, the AFM layer can induce a shift in the hysteresis loop of the FM layer along the magnetic field, giving rise to the exchange bias (ExB) effect.^[1] As a central ingredient in defining the magnetic reference states (“1” and “0”) of many spintronic and memory devices, the ExB effect has immense technological importance.^[2] Besides the unidirectional anisotropy, this effect is also characterized by several other physical variables and features, such as the blocking temperature,^[3] aging effect,^[4] memory effect,^[5] and increasing coercivity.^[6] In particular, the aging effect, measuring the decrease in the ExB effect as the number of consecutive hysteresis loops increases,^[4,7] is highly undesirable, because its presence will severely deteriorate the magnetic

C. Liu, D. Hou, Y. Liu, Z. Ma, Y. Sun, Z. Sheng
Anhui Key Laboratory of Condensed Matter Physics at Extreme Conditions
High Magnetic Field Laboratory
Hefei Institutes of Physical Science
Chinese Academy of Sciences
Hefei 230031, P. R. China
E-mail: zhigaosheng@hmf.ac.cn


C. Liu, S. Zhang, H. Wu, X. Li, Z. Zhang
The International Center for Quantum Design of Functional
Materials (ICQD)
University of Science and Technology of China
Hefei 230026, P. R. China
E-mail: zhangzy@ustc.edu.cn

H. Zhang, X. Xu
Key Laboratory of Magnetic Molecules and Magnetic Information
Materials of the Ministry of Education
Research Institute of Materials Science
Shanxi Normal University
Taiyuan 030000, P. R. China

Z. Jiang, X. Luo, Y. Sun
Key Laboratory of Materials Physics
Institute of Solid State Physics
Hefei Institutes of Physical Science
Chinese Academy of Sciences
Hefei 230031, P. R. China

H. Wang
Institute of Physics
Chinese Academy of Sciences
Beijing 100190, P. R. China

Z. Sheng
Key Laboratory of Photovoltaic Materials and Energy Conservation
Chinese Academy of Sciences
Hefei 230031, P. R. China

 The ORCID identification number(s) for the author(s) of this article can be found under <https://doi.org/10.1002/adma.202203411>.

DOI: 10.1002/adma.202203411

interfacial stability, and limit the durability of the devices in actual operations. Despite its widespread use and utmost technological importance, a full fundamental understanding of the ExB effect is still lacking.^[1,4] One of the major obstacle in gaining a better understanding of the phenomenon, is the low volume of the hetero-interface composed of conventional 3D materials, impeding direct observation and manipulation of the interfacial spin structure at the atomic scale.^[8–10] Another major and highly related roadblock is the complex and less controllable behaviors taking place at the interface, caused for example by lattice mismatch, interfacial diffusion, and other types of imperfections.^[11,12] Such limitations on its better understanding, in turn, prohibit full exploitation and utilization of the ExB effect.

Pleasantly, many of those difficulties inherently tied to 3D materials can be largely overcome upon the discoveries of 2D magnets.^[13–23] In particular, such 2D materials can be stacked into heterostructures with atomically precise interfacial control and weak (van der Waals) coupling, and their magnetic properties can be easily modulated by various external stimuli.^[24–32] These attributes make it possible to construct novel magnetic structures with unprecedented precision, properties, and applications, including FM/AFM structures that may harbor distinctly new ExB effect and allow its full explorations. Indeed, several recent studies have succeeded in fabricating heterostructures by stacking different 2D magnets or surface/interface modifications of 2D magnets, and further observed ExB effects.^[33–37]

In this paper, we report the discovery of an emergent, non-aging, extendable, and rechargeable ExB effect in a homostructural 2D magnet of Fe₃GeTe₂ (FGT). We first demonstrate, by utilizing straightforward moderate pressuring, that a FM-AFM transition is induced in the partial of a film sample, as confirmed by second harmonic generation (SHG) measurements and first-principles calculations. We then demonstrate that an FM/AFM heterointerface is established in the otherwise homostructure, as signified by the observation of distinct ExB effect in magneto-optical Kerr (MOKE) measurements. Strikingly, different from typical 3D systems, here the ExB effect exhibits negligible aging behavior upon repeated field cycling before its sudden collapse, via avalanching. Moreover, the ExB effect is shown to be able to stay stable over a much larger number of hysteresis loops by timed pressure repetition (extendability), and even recover after excessive training upon refreshed pressuring (rechargeability). The ExB effect in the present system also possesses versatile and broad tunability, with the bias field and observational temperature optimized to ≈1000 Oe and ≈130 K, respectively, viable for major practical applications. These central findings help to substantially enrich our fundamental understanding of the ExB effect and its training behaviors, and lay the device foundation for spintronics based on 2D materials.

2. Results and Discussion

The high-quality FGT single crystals were grown by the flux method (Figure S1, Supporting Information).^[38] The system has a centrosymmetric hexagonal structure of 6/mmm (*D*_{6h}) point group.^[39] Each unit cell is composed of two AB-stacked

FGT quintuple layers (Figure 1a), with weak van der Waals (vdW) interlayer coupling. The magnetization of the bulk FGT measured by the superconducting quantum interference device shows a Curie temperature $T_C \approx 200$ K and out-of-plane magnetic anisotropy (Figure S2, Supporting Information). Mechanical exfoliation via adhesive tape was applied to prepare the thin FGT nanoflakes, and such samples were transferred onto a SiO₂ substrate (Figure 1b). A large, clean, and single-domain area with homogeneous thickness enables high-precision spectroscopic characterizations using MOKE^[14,15] and SHG^[40,41] measurements as illustrated in Figure 1c.

As a reference system, a pristine FGT nanoflake (Figure 1b) possesses FM order, as confirmed by MOKE measurements (Figure 1d), showing a symmetric hysteresis loop with nearly-vertical jumps and large remanent magnetization at zero field.^[42] Such an FM order preserves spatial-inversion symmetry; accordingly, the system should not produce noticeable SHG response within the dominant electric dipole mechanism, as further confirmed in Figure 1e. Together, these measurements characterize the pristine FGT nanoflake as a uniform system with a single FM domain. Previous experimental studies have also identified that the spin coupling between neighboring FGT layers is ferromagnetic, even when the material is thinned down to the two-layer limit.^[16,17] Here, our strategy is to alter the FM coupling of the sample via simple mechanical pressuring, at least locally. Such a scenario, if accessible, will enable us to reach the ExB regime.

Indeed, this conjecture is unambiguously confirmed here with striking novelties and surprises. As illustrated in Figure 1f, a mild pressure of about 0.15 GPa along the *c* direction was applied to the nanoflake through polydimethylsiloxane (PDMS). Upon the removal of pressure, the sample was then cooled at zero field down to 10 K and the MOKE measurement reveals a distinct shift in the hysteresis loop (Figure 1g), signifying the emergence of the ExB effect. The magnitude of the ExB field, H_{ExB} , is about 450 Oe, which is comparable to that of the FGT-based heterostructures^[33–35] despite the distinctly superior homostructural nature of the present system. Remarkably, the ExB in the present homostructural system can be realized without cooling field, which is rarely seen in conventional ExB systems.^[42] The vdW nature with an atomically sharp interface, and the pressuring enhanced interlayer coupling warrant an uncompensated FM-AFM interface with single-domain homogeneity, essential for the onset of zero-field-cooling ExB. A similar phenomenon has also been reported recently in proton-intercalated FGT.^[33] Based on this understanding, we can apply a cooling field to guide the magnetization of the FM part and the interface, which in return gives rise to the ExB with pre-defined shifting direction. (Figure S3, Supporting Information).

The emergent ExB effect strongly points to the pressure induced FM-AFM transition as conjectured above. The presence of the AFM phase is likely to break the spatial-inversion symmetry, as confirmed by the SHG data shown in Figure 1h. Specifically, for the out-of-plane interlayer AFM configuration^[40] (inset of Figure 1g), the magnetic point group is the $3m$ (C_{3v}) = {*E*, $2C_3$, $3\sigma_v$ }, and the corresponding second-order susceptibility tensor has independent non-zero elements of $\chi_{yxx} = \chi_{xxy} = \chi_{xyx} = -\chi_{yyy}$. The experimental SHG data (red dots) is consistent with the fitting results (solid line) based on the

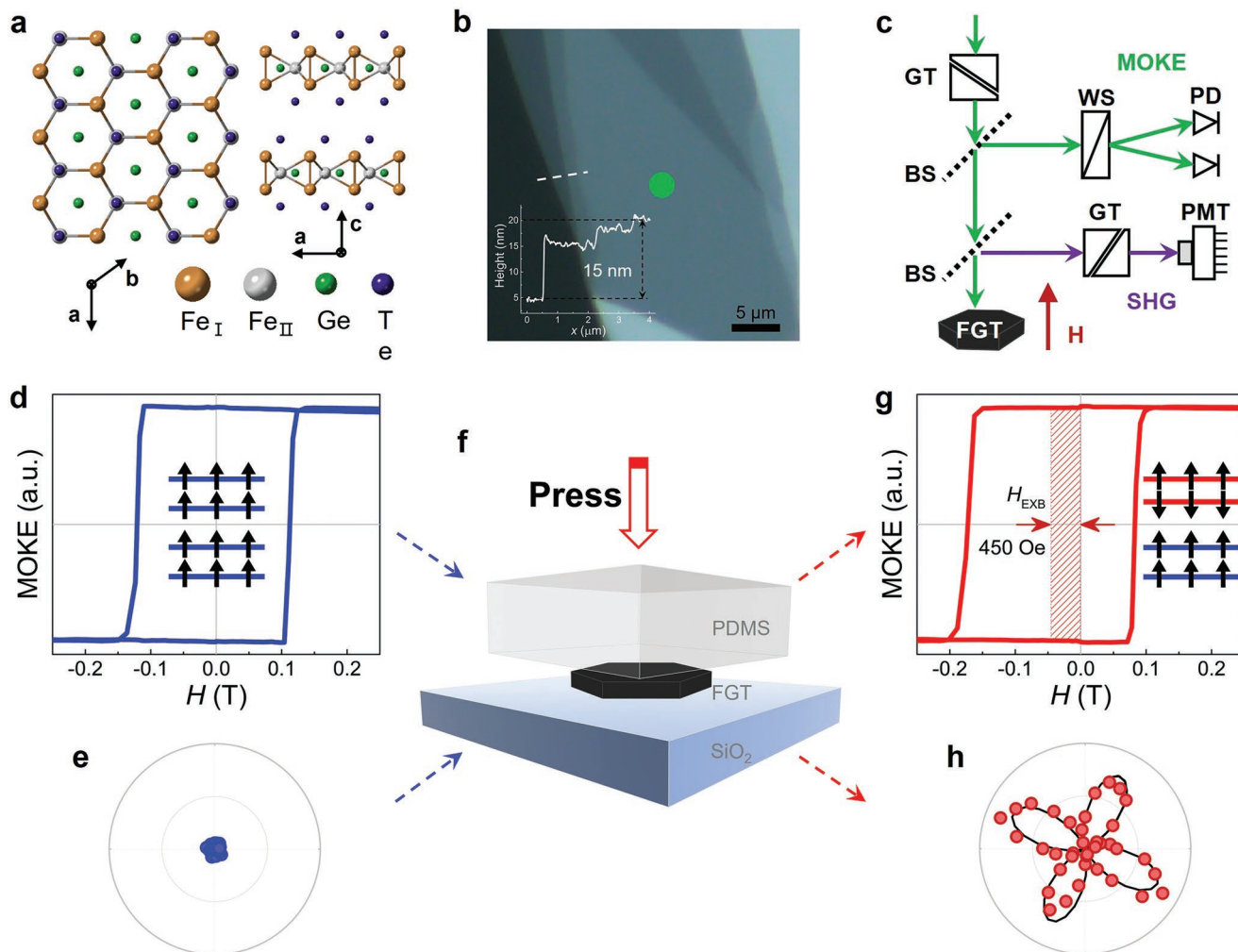


Figure 1. Atomic structure, optical image, MOKE/SHG geometry and data of the FGT samples. a) Top and side views of the atomic structure of layered FGT. b) Optical microscope image of a typical FGT flake on a SiO_2 substrate. The inset shows the thickness of the FGT flake measured by atomic force microscopy. The green dot highlights the central area of a large, flat terrace where the MOKE/SHG data was taken. c) Diagram of the polar MOKE and SHG measurements. Specifically, GT, BS, and WS here represent the Glan-Taylor Prism, beam splitter, and Wollaston splitter, respectively. PD and PMT here represent the balanced photodetection and photomultiplier tube, respectively. d) and e) Respective MOKE and SHG signals (with P_{out} geometry) of the pristine FGT at 10 K. f) Schematic of the mechanical pressuring. g,h) Respective MOKE and SHG signals (with P_{out} geometry) of the pressured FGT at 10 K.

AFM interlayer coupling (Figure 1h and Figure S4, Supporting Information). In addition, surface chemical characterization and controlled experiments further reveal that the emergent ExB effect in FGT is induced by pressuring, rather than surface oxidation (Figure S5 and S6, Supporting Information).

To gain further insights into the microscopic origin of the pressure-induced FM-AFM transition in the layered FGT, we use a bilayer FGT film as a model system to simulate the pressure effect by adjusting the interlayer distance based on first-principles calculations (Figure S7, Supporting Information). It is found that the energy difference (ΔE) between the FM and AFM couplings of FGT nanoflakes is rather small. Upon decreasing the interlayer distance, the AFM coupling becomes favored between adjacent FGT layers due to more significant enhancement of direct exchange compared with the super- and double-exchanges, as illustrated in a recent hydrostatic compression

experiment.^[43] With this important insight, we have further performed high-resolution transmission electron microscope (HRTEM) experiments to directly probe the structure change of the FGT upon pressuring (Figure S8, Supporting Information). The cross-section image of the pressured FGT clearly shows that, after the pressure is removed, the interlayer distance of the FGT sample exhibits an inhomogeneous distribution: the top layers are recovered back to the original value for pristine FGT (Figure 2a), while the bottom layers stay in a compressive state (Figure 2b), possibly due to residual stress or constraints from the substrate. The interlayer distances are distributed in a range crossing the critical value (≈ 8.0 Å according to our calculations) of the FM-AFM interlayer coupling (Figure 2c), further manifesting that an FM/AFM coexisting phases will develop in the post-pressured FGT. Furthermore, our theoretical results show that, whereas the pristine film (10-layers, closer to real

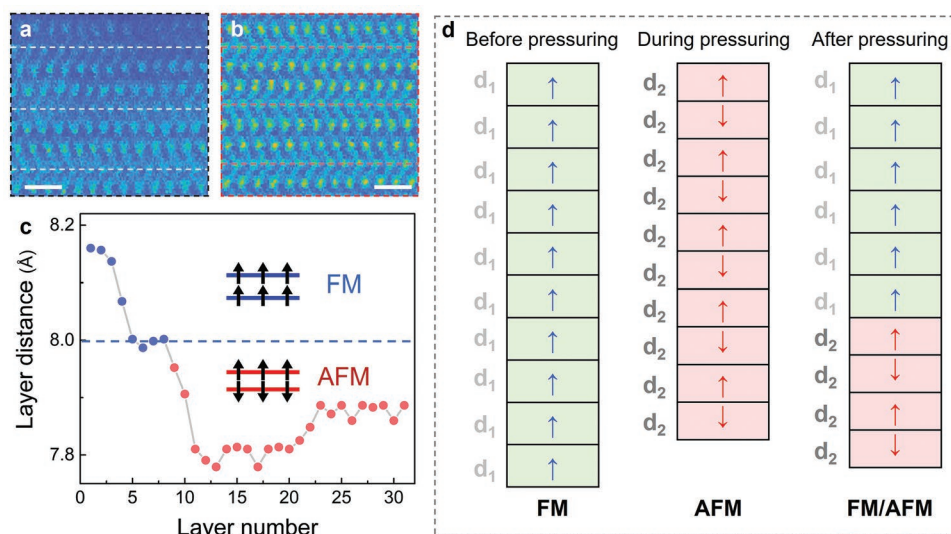


Figure 2. Structure of pressured FGT crystal. (a,b) are zoomed-in HRTEM images for the top and bottom layers, respectively. The scale bars are 5 Å. c) Distribution of the interlayer spacing of the post-pressured FGT sample with 31 layers in thickness. d) Schematic diagram of magnetic configuration of the FGT sample before, during, and after pressing. The interlayer distances $d_1 > 8$ Å and $d_2 < 8$ Å.

experiments) prefers FM interlayer coupling, the FM/AFM coexisting phase is energetically preferred to either the pure FM or AFM phase under a proper pressure (Figure S9, Supporting Information). Combining these experimental and computational results, we can deduce the evolution of interlayer spacing and coupling of the FGT sample upon pressing, as schematically illustrated in Figure 2d. These results indicate that even after the pressure is removed, the system in the FM/AFM coexisting phase is still (meta)stable enough to allow the MOKE/SHG measurements to be taken. These observations are informative in trying to understand the training effect of the ExB to be presented later. Here, we note that the quantitative difference between the experimentally applied and calculated pressures to reach the coexisting phase can be caused by the differences in various physical factors (such as the thickness), but the qualitative agreement is sound and valuable. We also note that, the moderate pressure needed to drive the FM/AFM coexisting phase to be the stable phase can be readily provided through proper packaging in practical device designs.

Now we proceed to characterize the temperature, pressure, and film thickness dependences of the ExB. First, with increasing temperature, the H_{ExB} gradually decreases from 450 Oe at 10 K to 174 Oe at 20 K, and vanishes when $T \geq 40$ K (Figure 3a). Consistently, the four-lobe SHG pattern extracted from the pressured FGT nanoflake shrinks sharply at $T \approx 40$ K (inset of Figure 3b). Above 40 K, the low SHG signal stays relatively flat, originating from the residual stress or nonmagnetic electric-quadrupole contribution at the FGT surface.^[41] These observations indicate that, either the Neel temperature for the AFM phase or the critical temperature for the decoupling between FM and AFM layers is ≈ 40 K, which is defined as T^* for simplicity. Here, T^* is far below $T_C \approx 200$ K of the pristine system, but can be substantially elevated for practical applications, as presented later. Secondly, the pressure dependence in a ≈ 15 -nm-thick FGT nanoflake shows that the ExB emerges only when the pressure is greater than 0.1 GPa, and the mag-

nitude of the H_{ExB} increases with pressure (Figure 3c,d). Pronouncedly, the H_{ExB} is drastically enhanced by three times, from 250 to 750 Oe, when the overall moderate pressure is increased from 0.1 to 0.23 GPa. Thirdly, the H_{ExB} is sensitive to the FGT thickness, increasing gradually as the nanoflake thickness decreases under the same pressing condition ($P = 0.23$ GPa and $T = 10$ K), reaching the practically valuable range of ≈ 1000 Oe at 12 nm (Figure S10, Supporting Information). Here it is also worthwhile to note that, the greater H_{ExB} that is reached for thinner nanoflakes is not only more desirable for robust device operations, but is also more beneficial for overall device miniaturization.

Next, we explore the characteristic behaviors of the ExB under repeated hysteresis cycling, focusing on the presence or absence of the aging effect as well as the training effect, the latter referring to the overall evolution of the ExB towards its complete annihilation. Here we recall that, in most FM/AFM heterostructures based on 3D materials, the H_{ExB} drops drastically from the first to the second cycle, and then decays gradually in subsequent cycles, and the phenomena are collectively known as the aging effect of ExB.^[1,5,44] The underlying reason has been attributed to magnetic configurational rearrangements at the FM/AFM interface caused by cycling. In stark contrast, the repeated MOKE loops of the pressured FGT homostructures display neither the initial drastic drop nor the observable decay in H_{ExB} , which still maintains at ≈ 420 Oe as the number of cycling n reaches ≈ 25 (Figure 4a). Such steady H_{ExB} unambiguously establishes the absence of the aging effect in those 2D FGT homostructures.

When the number of MOKE cycling is further increased ($n > 20$), the H_{ExB} of the 15-nm-thick FGT homostructures shows a sudden drop down to zero (Figure 4b). Such an avalanche mode of ExB annihilation is uniquely distinct, which has not been reported in any existing study of ExB phenomena. The corresponding SHG measurements further reveal that the ExB avalanche is accompanied by the disappearance of the AFM

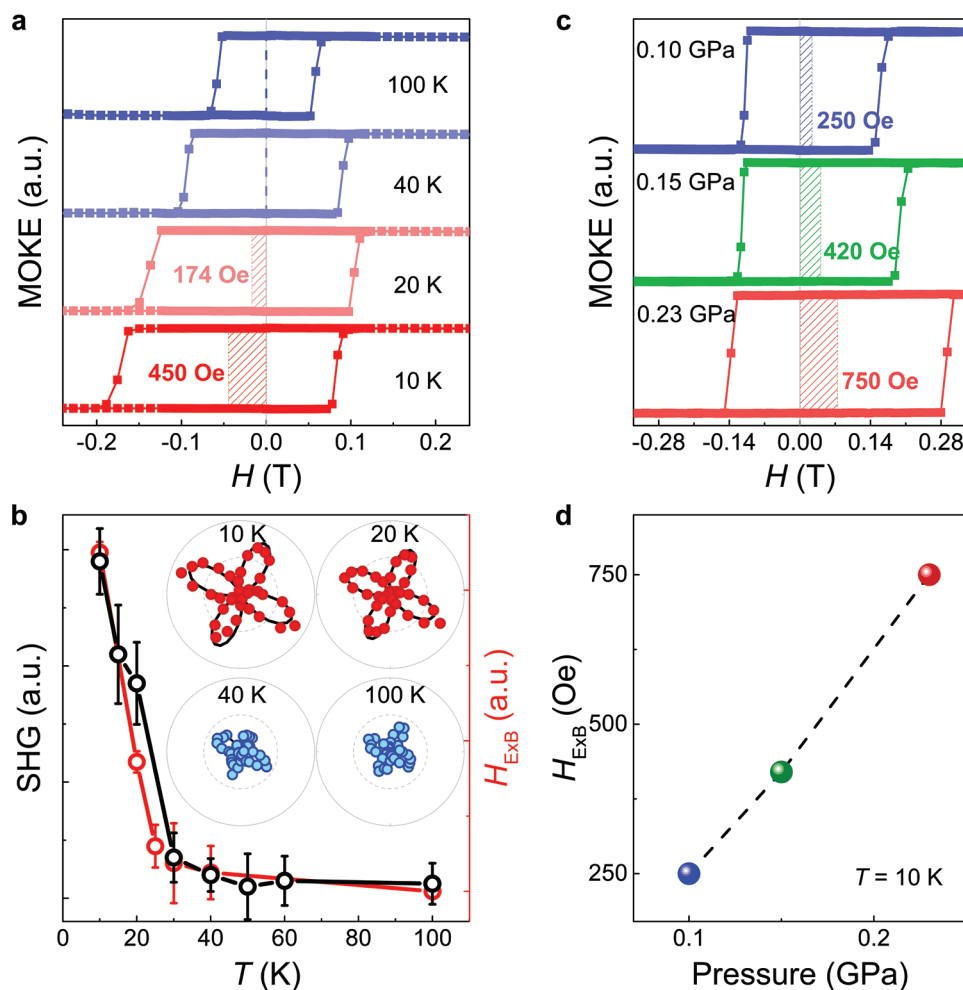


Figure 3. Temperature and pressure dependences of MOKE/SHG. a) Temperature-dependent MOKE signals of FGT. b) Temperature-dependent H_{ExB} and SHG responses of FGT. The inset images are the SHG patterns (with P_{out} geometry) at different temperatures. c) Pressure-dependent MOKE signals of FGT. d) Pressure-dependent H_{ExB} of FGT. All the samples used here have the thickness of 15 nm.

phase in the pressured FGT homostructure (Figure S11, Supporting Information), which is consistent with the metastable nature of the pressuring induced FM/AFM coexisting phase. Moreover, for a given sample, the ExB avalanching can be accelerated or delayed by different physical factors. For instance, with increasing strength of the sweeping magnetic field, the avalanche will take place sooner, and in the high-field limit, the critical number of the cycling defined by the avalanching, n_c , can be reduced down to 1 (Figure S12, Supporting Information). On the other hand, it is natural to expect that lowering the temperature will delay the avalanching.

Beyond the finer tunabilities on n_c discussed above, here we demonstrate that the lack of aging effect in the present system allows to drastically increase n_c , in principle to any desirable value for practical applications. The feasibility of such an ultimate goal is demonstrated via repeated and properly timed pressuring, as shown in Figure 4c. Here, a pressure of 0.23 GPa is applied to a 25-nm-thick nanoflake with $n_c \approx 22$ (Figure S13, Supporting Information) before the cycling of $n = 1, 16,$ and 31. Strikingly, we observe non-aging ExB effect without avalanching, indicating that n_c has been effectively delayed to

more than 45. These results demonstrate that timed pressure repetition can effectively extend the survival time of the pressure-induced AFM phase, and avoid the ExB avalanche of the vdW homostructures. Intuitively, the repeated pressuring operation can be viewed as a way to replenish the “mechanomagnetic energy” needed to stabilize the FM/AFM coexisting phase of the homostructure, thereby extending the ExB effect and ensuring the durability of the device operations.

In addition to the extendability, another salient feature of the present system is the rechargeability of the ExB effect after the avalanche. As shown in Figure 4d, after the first pressuring with 0.15 GPa, the ExB effect emerges in a 25-nm-thick nanoflake, with $n_c = 21$. Afterwards, a second pressure of 0.23 GPa is applied to the avalanched system, which recovers the ExB at higher H_{ExB} . These results not only demonstrate the rechargeability of the ExB, but also the tunability of its magnitude. Collectively, the present study demonstrates that the very vdW homostructural nature of such 2D FGT systems enables them to serve as dream platforms, allowing simple approaches, such as moderate pressuring, to be a powerful knob in revealing unprecedentedly rich physics surrounding the ExB effect.

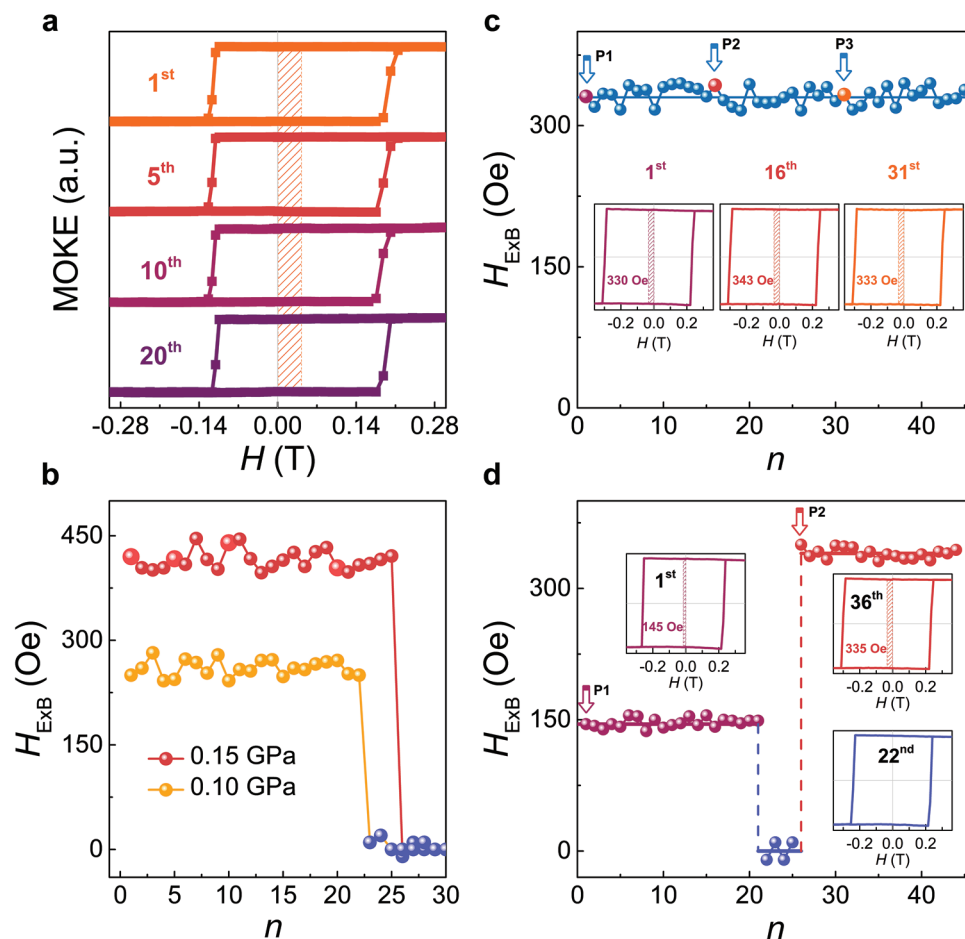


Figure 4. Training, avalanching, extendability and rechargeability of the ExB. a) Repeated magnetic cycling results in a 15-nm-thick FGT homostructure, with the cycling numbers marked in (b). b) Training effect of the H_{ExB} versus n of two representative pressured FGT samples, both with 15-nm thickness. c) “Extendable” H_{ExB} versus n of an FGT homostructure. The arrows “P1”, “P2”, and “P3” mark the first, second, and third pressuring, respectively. The insets display the 1st, 16th, and 31st hysteresis loops, respectively. d) “Rechargeable” H_{ExB} versus n of an FGT homostructure, in which the ExB effect is recovered via a second pressuring after the avalanche. The insets display the 1st, 22nd, and 36th hysteresis loops, respectively.

At present, the underlying microscopic origins for both the absence of the aging effect and the avalanching mode of the overall training effect, as striking, original, and technologically important as they are, remain to be precisely identified. Nevertheless, some lights can be shed on each of them, especially in comparison with ExB effects in 3D systems. In traditional 3D systems, the interfaces defined by strong chemical bonding typically suffer from various imperfections, such as roughness induced magnetic frustration,^[1] existence of multiple easy magnetization axes,^[45] and defect induced magnetic dilution,^[46] which have been suggested as the sources of the aging effect. In contrast, the typical 2D heterostructures formed by two different materials with vdW coupling^[8–10] in principle will possess overall improved interface quality over the 3D counterparts. Even so, such systems still exhibit pronounced aging effect in the ExB.^[33] Going one major step further, the 2D FGT homostructures created here via simple pressuring naturally possess perfectly clean interfaces, which are predominantly defined by their magnetically different configurations. Such cleanness and atomic structural perfection are likely the defining factors, allowing the non-aging ExB as observed. To support on this

conjecture and gain some supplementary insights, we have constructed a FM-AFM composite model system with homogeneous interfacial coupling and a single easy magnetization axis, and simulated its magnetization dynamics. The results confirm the robustness of the H_{ExB} upon multiple cyclings (Figure S14, Supporting Information). As for the avalanching mode, its physical origin must be tied to the metastable nature of the FM/AFM coexisting phase reached by pressuring. In this regard, we note an important observation that, the pressured sample that exhibits the ExB is well preserved at 10 K for a full day without magnetic cycling, and afterwards still exhibit essentially the same ExB effect if measured again (Figure S15, Supporting Information), further indicating the sufficient metastability of such pressured samples. Based on this observation, we can conjecture the triggering of the avalanche to coincide with the critical accumulation of the “magneto-mechanical energy” introduced by the magnetic sweeping towards the globally stable phase, where the whole system restores its FM state. Such an exotic phase transition may harbor intriguing physical characteristics in its own right,^[47,48] which are to be fully explored.

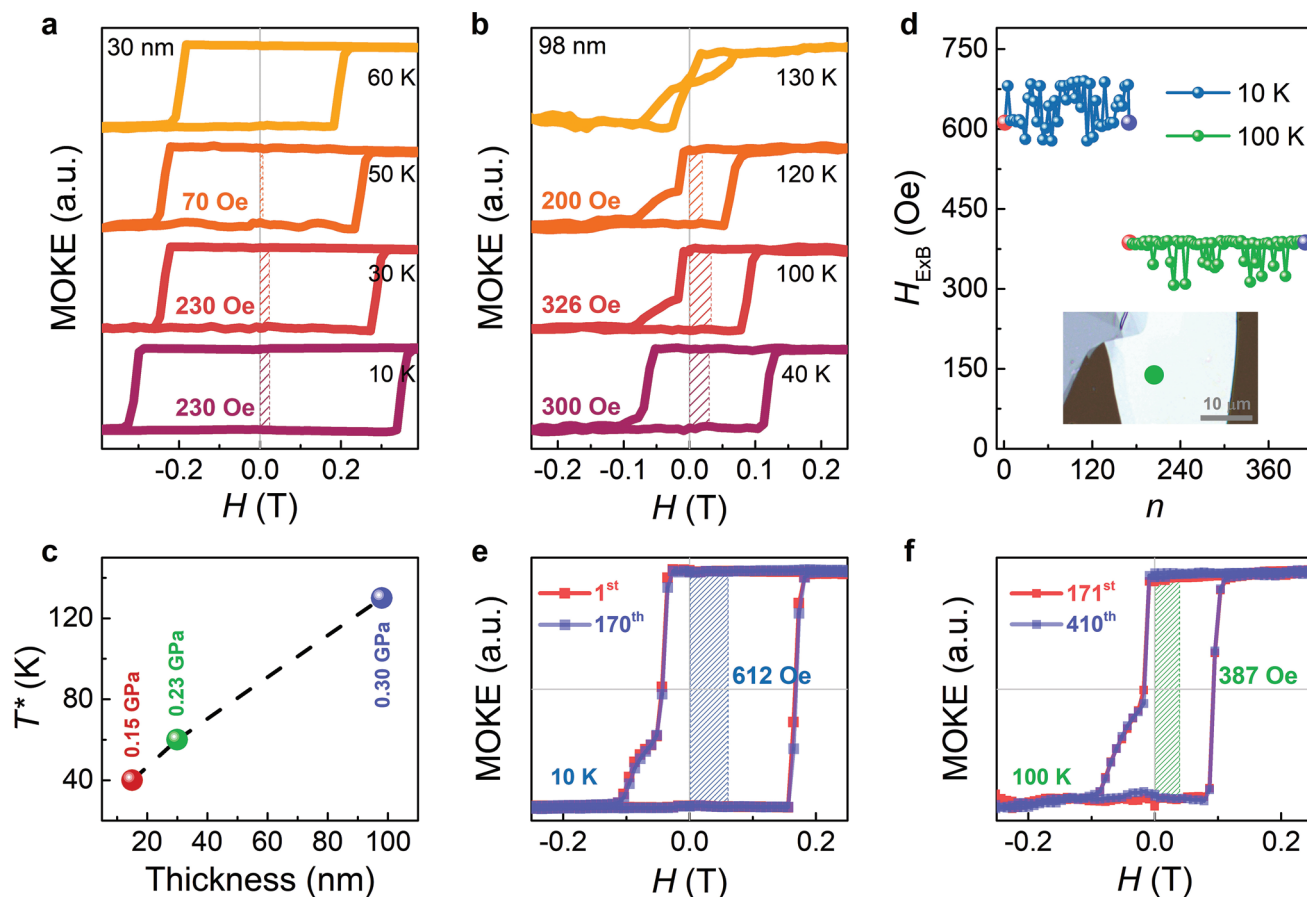


Figure 5. Drastically enhanced T^* and much prolonged ExB cycles of thicker FGT homostructures. a,b) Temperature-dependent MOKE signals of 30-nm and 98-nm thick FGT nanoflakes, pressured at 0.23 and 0.30 GPa, respectively, with corresponding $T^* \approx 60$ K and 130 K. c) Evolution of T^* with the sample thickness and pressure. d) Lack of the training effect in the ExB cycling of the 98-nm thick nanoflake taken at the low (10 K) and high (100 K) temperatures. The insert also illustrates the optical image of the sample. For better clarity, for a given temperature, only every fourth data point is plotted between the first and last data points. e,f) The essentially identical hysteresis loops for the first and last magnetic cyclings at the respective low and high temperatures.

So far, we have focused on thinner homostructures (<25 nm), allowing us to reveal novel and rich phenomena surrounding the emergent ExB, especially its non-aging and avalanching characteristics. Going beyond such fundamental aspects, a clear technological drive is to exploit these materials for device applications. In this regard, the relatively low $T^* \approx 40$ K may pose severe limitations. In addressing this issue, we reflect that pressuring induced AFM phase becomes metastable after load removal (Figure 2d), and the metastability defining the T^* should be tunable by various physically controllable parameters, making T^* tunable as well. Since the metastability should be dependent on the thickness of the AFM phase (namely, the thicker, the more (meta)stable), we use thicker samples to verify this expectation, as such samples can endure higher pressures while still preserving the FM component. As illustrated in Figure 5, the results are in essence spectacular, in that the T^* can be elevated to 130 K (and likely even higher), and that for the thickest sample tested, the avalanching is not even in sight within the number of cyclings we have taken. The T^* values of all the studied samples are plotted in Figure 5c, showing a clear and strong thickness dependence. In principle, T^* can be fur-

ther increased in such homostructural systems, provided that a more stable antiferromagnetic phase can be induced and preserved. However, for samples thicker than 100 nm, the required magnitude of pressure exceeds the reach of the present PDMS-assisted scheme, leaving this technologically significant aspect to be explored in future studies with potentially alternative pressuring schemes. It is also conceptually intriguing to conduct continuous experiments to identify the value of n_c , which must be finite based on physical considerations, but here it suffices to emphasize that the striking findings in the present study make these materials viable platforms for the broad range of practical applications.

3. Conclusions

As broader perspectives, we emphasize that the straightforward pressuring scheme and design principle of the ultraclean homostructural systems demonstrated here, are readily extendable to other fertile vdW magnetic materials discovered recently, wherein the ExB is envisioned to exhibit system-specific

novelties and characteristics. The central findings of the present study should also stimulate intensive research efforts on gaining a full understanding of microscopic mechanisms responsible for the striking and coherently connected phenomena surrounding the ExB. Lastly, the large magnitudes of the H_{ExB} achieved in the current FGT homostructures, coupled with the compelling non-aging, extendable, and rechargeable features, constitute a major step forward, with immense practical applications in sight.

4. Experimental Section

Fabrication of FGT Homostructure Via Uniaxial Pressuring: A micromanipulator (Metatest, E1-T) was used, combining PDMS, to apply the pressure on the FGT nanflakes (Figures S16–S19, Supporting Information). First, a target FGT flake was mechanically exfoliated from bulk crystals and then transferred onto a quartz substrate (SiO_2 , Prmat Technology). In parallel, a glass slide with the PDMS was inserted and attached to the micromanipulator. Second, the PDMS was slowly lowered and pressured against onto the target FGT flake by the micromanipulator. Upon pressuring, the PDMS first experiences an inelastic deformation, with the thickness shrinking and the lateral area expanding slightly, and then behaves like a rigid media effectively transferring the applied force to the sample (See Figure S16, Supporting Information, for a schematic illustration), as confirmed by the force sensing measurement from the substrate (Figure S17, Supporting Information). The PDMS layer was essential in the pressuring experiments. Unlike rigid media such as tungsten tips (Figure S18, Supporting Information), it will not damage the sample throughout the pressuring process (Figures S19, Supporting Information). The scars left by this polymer after heating also provide a convenient way to determine the pressuring area. The force (fixed as 36 N) was provided by the micromanipulator, whereas the contact area between the target FGT and PDMS could be adjusted in the range of 0.12–4 mm². Hence, the pressure applied on the FGT nanoflakes could be modulated from 0.01 to 0.3 GPa. After pressuring for three minutes, the substrate was heated to 40 °C and then the PDMS was lifted to obtain the pressured FGT flake. Such sample preparation experiments (including exfoliation, transfer, and pressurization) were carried out in Ar-filled glovebox ($\text{O}_2 < 0.1$ ppm and $\text{H}_2\text{O} < 0.1$ ppm). Then, the samples were extracted from the glovebox and immediately transferred to the high-vacuum cryostat ($< 10^{-5}$ Pa) with argon protection. In addition, the sample preparation experiments were also carried out in air conditions, and almost identical ExB effects were observed in the pressured FGT samples, which identifies the plausible air-stability of the FGT.

HRTEM Measurements: The cross-sectional samples were first obtained from the pressured FGT samples using focused ion beam (Zeiss crossbeam 540). The atomic structure analysis was then carried out on the cross-sectional samples using high-angle annular dark-field images, which were acquired in scanning mode on a transmission electron microscope equipped with double Cs correctors for the condenser and objective lenses (ARM300F, JEOL), and a cold field emission gun at 300 kV.

Optical MOKE and SHG Measurements: The MOKE and SHG measurements were conducted in a low-vibration high-vacuum ($< 10^{-5}$ Pa) cryostat (ARS, CS204SF-FMX-20) with a minimum temperature of 10 K. The magnetic field, perpendicular to the sample surface with magnitude up to 0.65 T, was provided by an electromagnet. The normal incident geometry with a 50× non-magnetic objective (CCW-50, PDV) was utilized, and the focused laser beam size was around 1 μm on the chosen areas of the nanoflakes. For the MOKE measurement, a power-stabilized continuous wave laser with wavelength ≈532 nm was incident to the sample, and the reflected light was collected by a rotatable balance detector equipped with a Wollaston prism to detect the MOKE signal. For the SHG measurement, a femtosecond laser (Ti: sapphire laser, 800 nm, 100 fs, 84 MHz) was focused on the sample

surface and the reflected SHG photons (400 nm) were detected by a photomultiplier tube.

SHG Pattern Fitting: The nonzero elements for the electric polar tensor, χ_{ijk} , for the point group $3m$ (C_{3v}) are

$$\begin{bmatrix} 0 & 0 & 0 & 0 & \chi_{zxz} & \chi_{xzy} \\ \chi_{yxx} & \chi_{yyy} & 0 & \chi_{yyz} & 0 & 0 \\ \chi_{zxx} & \chi_{zyy} & \chi_{zzz} & 0 & 0 & 0 \end{bmatrix} \quad (1)$$

The SHG experiment was performed in back-scattering geometry, where incident and emitted lights propagate in -z and z directions, respectively. For such geometry, there is no SHG output contribution form z component. As a result, the SHG intensity in parallel (XX) and perpendicular (XY) polarization geometry can be given by

$$I_{\parallel}(2\omega, \alpha) \propto \left[\chi_{yyy} \sin^3 \alpha + (\chi_{yxz} + 2\chi_{xzy}) \sin \alpha \cos^2 \alpha \right]^2 \quad (2)$$

$$I_{\perp}(2\omega, \alpha) \propto \left[\chi_{yxz} \cos^3 \alpha + (\chi_{yyy} - 2\chi_{xzy}) \cos \alpha \sin^2 \alpha \right]^2 \quad (3)$$

where ω is the frequency, and α is the azimuthal angle between the polarization of the input field and the crystallographic x coordinate.

First-Principles Calculations: First-principles calculations based on density functional theory (DFT) were performed to calculate the total energies of FM and AFM FGT by utilizing the Vienna ab initio simulation package.^[33] The projector augmented wave method was used to handle the core electron states. The generalized gradient approximation and the Perdew-Burke-Ernzerhof functional were employed to model the electron exchange, and correlation interactions. The valence electron wave functions were expanded by a plane-wave basis with the cutoff energy of 400 eV. The structure optimization was carried out using the conjugate-gradient algorithm. All the atoms were relaxed until the Hellmann–Feynman force on each atom was smaller than 0.01 eV Å⁻¹. The *T*-centered Monkhorst–Pack k-point meshes of 24 × 24 × 1 were adopted for layered FGT. The vdW interactions were considered in the calculations with the Grimme's DFT-D2 method.

Simulation of vdW ExB System: To simulate the ExB effect at a clean FM-AFM interface, an AA-stacked four-layer spin lattice with periodic and open boundary in the lateral and vertical directions, respectively, was designed. Each constituent layer was modeled by a 20 × 20 supercell of square lattice, with FM coupling between nearest neighboring sites. The top and bottom two layers were defined as the AFM and FM regions, respectively, with a homogeneous interface in between. The out-of-plane direction pointing from the FM to AFM region was defined as the positive field direction. The spin Hamiltonian reads,

$$H = -A \sum_i S_{iz}^2 - \mu_B \sum_i \vec{S}_i \cdot \vec{B} - J_{\text{in-plane}} \sum_{\langle i,j \rangle} \vec{S}_i \cdot \vec{S}_j \quad (4)$$

$$- J_{\text{FM}} \sum_{\langle i,j \rangle}^{i,j \in \text{FM}} \vec{S}_i \cdot \vec{S}_j - J_{\text{AF}} \sum_{\langle i,j \rangle}^{i,j \in \text{AFM}} \vec{S}_i \cdot \vec{S}_j - J_{\text{inter}} \sum_{\langle i,j \rangle}^{i \in \text{FM}, j \in \text{AFM}} \vec{S}_i \cdot \vec{S}_j \quad (5)$$

Here, the first and second terms correspond to the single-ion anisotropy and Zeeman field, respectively. The third term was the intra-layer coupling between nearest sites; the last three terms represent the couplings between adjacent layers within the FM region, the AFM regions, and at the interface, respectively. It was set $S = 1$, $A = 0.2$ meV, $J_{\text{in-plane}} = 1.0$ meV, $J_{\text{FM}} = J_{\text{inter}} = 0.1$ meV, and $J_{\text{AF}} = -0.5$ meV. Such parameterization enabled the model to capture essential features of the FGT-based homostructure, such as the large out-of-plane anisotropy and strong intra-layer ferromagnetism confirmed by previous studies,^[16,17] and the FM/AFM coexisting phase with clean interface discovered in the present work. The magnetization dynamics was simulated by numerically integrating the Landau-Lifshitz-Gilbert equation^[49] with respect to time, as implemented in the Spirit code.^[50] The time step

was 0.1 ps, and the spin lattice was relaxed for 500 ps at 5 K under each sweeping fields.

Supporting Information

Supporting Information is available from the Wiley Online Library or from the author.

Acknowledgements

C.X.L., H.S.Z. and S.H.Z. contributed equally to this work. The authors gratefully acknowledge financial support from the National Key R&D Program of China (Grant No. 2021YFA1600200, 2017YFA0303603, 2017YFA0303500, and 2017YFB0405703), the National Natural Science Foundation of China (NSFC; Grant No. U2032218, 11904350, 11634011, 11974323, 11722435, 11804210, 11904367, and 51871137), the Plan for Major Provincial Science & Technology Project (Grant No. 202003a05020018), the Key Research Program of Frontier Sciences, CAS (Grant No. QYZDB-SSW-SLH011), the Users with Excellence Program of Hefei Science Center CAS (Grant No. 2021HSC-UE009), and the President's fund of Hefei Research Institute (Grant No. YZJJ2022QN37). The Strategic Priority Research Program of Chinese Academy of Sciences (Grant No. XDB30000000), the Anhui Initiative in Quantum Information Technologies (Grant No. AHY170000), and Anhui Provincial Natural Science Foundation (Grant No. 2008085QA30 and 2008085QA44). A portion of this work was performed on the Steady High Magnetic Field Facilities, High Magnetic Field Laboratory, CAS, and supported by the High Magnetic Field Laboratory of Anhui Province.

Conflict of Interest

The authors declare no conflict of interest.

Data Availability Statement

The data that support the findings of this study are available from the corresponding author upon reasonable request.

Keywords

2D magnets, exchange bias, Fe₃GeTe₂, training effect, van der Waals homostructures

Received: April 15, 2022
Revised: October 13, 2022
Published online: November 18, 2022

- [1] J. Nogues, I. K. Schuller, *J. Magn. Magn. Mater.* **1999**, *192*, 203.
- [2] Z. Luo, T. P. Dao, A. Hrabec, J. Vijayakumar, A. Kleibert, M. Baumgartner, E. Kirk, J. Cui, T. Savchenko, G. Krishnaswamy, L. J. Heyderman, P. Gambardella, *Science* **2019**, *363*, 1435.
- [3] M. Gibert, P. Zubko, R. Scherwitzl, J. Iniguez, J.-M. Triscone, *Nat. Mater.* **2012**, *11*, 195.
- [4] S. Brems, K. Temst, C. V. Haesendonck, *Phys. Rev. Lett.* **2007**, *99*, 067201.
- [5] M. Kiwi, *J. Magn. Magn. Mater.* **2001**, *234*, 584.
- [6] E. Lachman, R. A. Murphy, N. Maksimovic, R. Kealhofer, S. Haley, R. D. McDonald, J. R. Long, J. G. Analytis, *Nat. Commun.* **2020**, *11*, 560.

- [7] T. Hauet, J. A. Borchers, P. Mangin, Y. Henry, S. Mangin, *Phys. Rev. Lett.* **2006**, *96*, 067207.
- [8] K. S. Novoselov, A. Mishchenko, A. Carvalho, A. H. Castro Neto, *Science* **2016**, *353*, 9439.
- [9] K. S. Burch, D. Mandrus, J.-G. Park, *Nature* **2018**, *563*, 47.
- [10] C. Gong, X. Zhang, *Science* **2019**, *363*, 706.
- [11] X. Liu, M. C. Hersam, *Adv. Mater.* **2018**, *30*, 1801586.
- [12] D. Rhodes, S. H. Chae, R. Ribeiro-Palau, J. Hone, *Nat. Mater.* **2019**, *18*, 541.
- [13] J.-U. Lee, S. Lee, J. H. Ryoo, S. Kang, T. Y. Kim, P. Kim, C.-H. Park, J. G. Park, H. Cheong, *Nano Lett.* **2016**, *16*, 7433.
- [14] C. Gong, L. Li, Z. L. Li, H. W. Ji, A. Stern, Y. Xia, T. Cao, W. Bao, C. Z. Wang, Y. A. Wang, Z. Q. Qiu, R. J. Cava, S. G. Louie, J. Xie, X. Zhang, *Nature* **2017**, *546*, 265.
- [15] B. Huang, G. Clark, E. Navarro-Moratalla, D. R. Klein, R. Cheng, K. L. Seyler, D. Zhong, E. Schmidgall, M. A. McGuire, D. H. Cobden, W. Yao, D. Xiao, P. Jarillo-Herrero, X. D. Xu, *Nature* **2017**, *546*, 270.
- [16] Y. Deng, Y. Yu, Y. Song, J. Zhang, N. Z. Wang, Z. Sun, Y. Yi, Y. Z. Wu, S. Wu, J. Zhu, J. Wang, X. H. Chen, Y. Zhang, *Nature* **2018**, *563*, 94.
- [17] Z. Fei, B. Huang, P. Malinowski, W. Wang, T. Song, J. Sanchez, W. Yao, D. Xiao, X. Zhu, A. F. May, W. Wu, D. H. Cobden, J.-H. Chu, X. Xu, *Nat. Mater.* **2018**, *17*, 778.
- [18] D. R. Klein, D. MacNeill, J. L. Lado, D. Soriano, E. Navarro-Moratalla, K. Watanabe, T. Taniguchi, S. Manni, P. Canfield, J. Fernandez-Rossier, P. Jarillo-Herrero, *Science* **2018**, *360*, 1218.
- [19] L. B. Chen, J.-H. Chung, B. Gao, T. Chen, M. B. Stone, A. I. Kolesnikov, Q. Huang, P. Dai, *Phys. Rev. X* **2018**, *8*, 041028.
- [20] C. Tan, J. Lee, S.-G. Jung, T. Park, S. Albarakati, J. Partridge, M. R. Field, D. G. McCulloch, L. Wang, C. Lee, *Nat. Commun.* **2018**, *9*, 1554.
- [21] W. Chen, Z. Sun, Z. Wang, L. Gu, X. Xu, S. Wu, C. Gao, *Science* **2019**, *366*, 983.
- [22] L. Thiel, Z. Wang, M. A. Tschudin, D. Rohner, I. Gutierrez-Lezama, N. Ubrig, M. Gibertini, E. Giannini, A. F. Morpurgo, P. Maletinsky, *Science* **2019**, *364*, 973.
- [23] T. Song, Q. C. Sun, E. Anderson, C. Wang, J. Qian, T. Taniguchi, K. Watanabe, M. A. McGuire, R. Stohr, D. Xiao, T. Cao, J. Wrachtrup, X. Xu, *Science* **2021**, *374*, 1140.
- [24] T. C. Song, X. Cai, M. W.-Y. Tu, X. Zhang, B. Huang, N. P. Wilson, K. L. Seyler, L. Zhu, T. Taniguchi, K. Watanabe, M. A. McGuire, D. H. Cobden, D. Xiao, W. Yao, X. Xu, *Science* **2018**, *360*, 1214.
- [25] S. Jiang, J. Shan, K. F. Mak, *Nat. Mater.* **2018**, *17*, 406.
- [26] Q. Li, M. Yang, C. Gong, R. V. Chopdekar, A. T. N'Diaye, J. Turner, G. Chen, A. Schol, P. Shafer, E. Arenholz, A. K. Schmid, S. Wang, K. Liu, N. Gao, A. S. Admasu, S.-W. Cheong, C. Hwang, J. Li, F. Wang, X. Zhang, Z. Qiu, *Nano Lett.* **2018**, *18*, 5974.
- [27] Z. Wang, T. Zhang, M. Ding, B. Dong, Y. Li, M. Chen, X. Li, J. Huang, H. Wang, X. Zhao, Y. Li, D. Li, C. Jia, L. Sun, H. Guo, Y. Ye, D. Sun, Y. Chen, T. Yang, J. Zhang, S. Ono, Z. Han, Z. Zhang, *Nat. Nanotechnol.* **2018**, *13*, 554.
- [28] T. Li, S. Jiang, N. Sivadas, Z. Wang, Y. Xu, D. Weber, J. E. Goldberger, K. Watanabe, T. Taniguchi, C. J. Fennie, K. F. Mak, J. Shan, *Nat. Mater.* **2019**, *18*, 1303.
- [29] T. Song, Z. Fei, M. Yankowitz, Z. Lin, Q. Jiang, K. Hwangbo, Q. Zhang, B. Sun, T. Taniguchi, K. Watanabe, M. A. McGuire, D. Graf, T. Cao, J.-H. Chu, D. H. Cobden, C. R. Dean, D. Xiao, X. Xu, *Nat. Mater.* **2019**, *18*, 1298.
- [30] B. Liu, S. Liu, L. Yang, Z. Chen, E. Zhang, Z. Li, J. Wu, X. Ruan, F. Xiu, W. Liu, L. He, R. Zhang, Y. Xu, *Phys. Rev. Lett.* **2020**, *125*, 267205.
- [31] Y. Wang, C. Wang, S.-J. Liang, Z. Ma, K. Xu, X. Liu, L. Zhang, A. S. Admasu, S.-W. Cheong, L. Wang, M. Chen, Z. Liu, B. Cheng, W. Ji, F. Miao, *Adv. Mater.* **2020**, *32*, 2004533.
- [32] S. Li, Z. Ye, X. Luo, G. Ye, H. Kim, B. Yang, S. Tian, C. Li, H. Lei, A. W. Tsen, K. Sun, R. He, L. Zhao, *Phys. Rev. X* **2020**, *10*, 011075.

- [33] G. Zheng, W.-Q. Xie, S. Albarakati, M. Algarni, C. Tan, Y. Wang, J. Peng, J. Partridge, L. Farrar, J. Yi, Y. Xiong, M. Tian, Y.-J. Zhao, L. Wang, *Phys. Rev. Lett.* **2020**, 125, 047202.
- [34] R. Zhu, W. Zhang, W. Shen, P. K. J. Wong, Q. Wang, Q. Liang, Z. Tian, Y. Zhai, C.-W. Qiu, A. T. S. Wee, *Nano Lett.* **2020**, 20, 5030.
- [35] H. K. Gweon, S. Y. Lee, H. Y. Kwon, J. Jeong, H. J. Chang, K.-W. Kim, Z. Q. Qiu, H. Ryu, C. Jang, J. W. Choi, *Nano Lett.* **2021**, 21, 1672.
- [36] J. Jo, F. Calavalle, B. Martin-Garcia, D. Tezze, F. Casanova, A. Chuvilin, L. E. Hueso, M. Gobbi, *Adv. Mater.* **2022**, 34, 2200474.
- [37] Y. Wu, W. Wang, L. Pan, K. L. Wang, *Adv. Mater.* **2022**, 34, 2105266.
- [38] H.-J. Deiseroth, K. Aleksandrov, C. Reiner, L. Kienle, R. K. Kremer, *Eur. J. Inorg. Chem.* **2006**, 2006, 1561.
- [39] Y. Wang, C. Xian, J. Wang, B. Liu, L. Ling, L. Zhang, L. Cao, Z. Qu, Y. Xiong, *Phys. Rev. B* **2017**, 96, 134428.
- [40] Z. Sun, Y. Yi, T. Song, G. Clark, B. Huang, Y. Shan, S. Wu, D. Huang, C. Gao, Z. Chen, M. McGuire, T. Cao, D. Xiao, W.-T. Liu, W. Yao, X. Xu, S. Wu, *Nature* **2019**, 572, 497.
- [41] H. Chu, C. J. Roh, J. O. Island, C. Li, S. Lee, J. Chen, J.-G. Park, A. F. Young, J. S. Lee, D. Hsieh, *Phys. Rev. Lett.* **2020**, 124, 027601.
- [42] B. M. Wang, Y. Liu, P. Ren, B. Xia, K. B. Ruan, J. B. Yi, J. Ding, X. G. Li, L. Wang, *Phys. Rev. Lett.* **2011**, 106, 077203.
- [43] S. Ding, Z. Liang, J. Yang, C. Yun, P. Zhang, Z. Li, M. Xue, Z. Liu, G. Tian, F. Liu, W. Wang, W. Yang, J. Yang, *Phys. Rev. B* **2021**, 103, 094429.
- [44] C. Binek, S. Polisetty, X. He, A. Berger, *Phys. Rev. Lett.* **2006**, 96, 067201.
- [45] A. Hoffmann, *Phys. Rev. Lett.* **2004**, 93, 097203.
- [46] U. Nowak, K. D. Usadel, J. Keller, P. Miltenyi, B. Beschoten, G. Guntherodt, *Phys. Rev. B* **2002**, 66, 014430.
- [47] P. Bak, C. Tang, K. Wiesenfeld, *Phys. Rev. Lett.* **1987**, 59, 381.
- [48] S. R. Nagel, *Rev. Mod. Phys.* **1992**, 64, 321.
- [49] T. L. Gilbert, *IEEE Trans. Magn.* **2004**, 40, 3443.
- [50] G. P. Muller, M. Hoffmann, C. Disselkamp, D. Schurhoff, S. Mavros, M. Sallermann, N. S. Kiselev, H. Jonsson, S. Blugel, *Phys. Rev. B* **2019**, 99, 224414.